REPORTS

INDUCED SEISMICITY

Seismicity triggered by fluid injection–induced aseismic slip

Yves Guglielmi,[1]* Frédéric Cappa,[2,3] Jean-Philippe Avouac,[3]† Pierre Henry,[1] Derek Elsworth[4]

Anthropogenic fluid injections are known to induce earthquakes. The mechanisms involved are poorly understood, and our ability to assess the seismic hazard associated with geothermal energy or unconventional hydrocarbon production remains limited. We directly measure fault slip and seismicity induced by fluid injection into a natural fault. We observe highly dilatant and slow [~4 micrometers per second (μm/s)] aseismic slip associated with a 20-fold increase of permeability, which transitions to faster slip (~10 μm/s) associated with reduced dilatancy and micro-earthquakes. Most aseismic slip occurs within the fluid-pressurized zone and obeys a rate-strengthening friction law $\mu = 0.67 + 0.045\ln\left(\frac{v}{v_0}\right)$ with v_0 = 0.1 μm/s. Fluid injection primarily triggers aseismic slip in this experiment, with micro-earthquakes being an indirect effect mediated by aseismic creep.

Injection of fluid into the crust can generate seismicity, with source mechanisms similar to natural earthquakes and occasionally large enough to cause damage (*1*–*6*). Induced seismicity is generally regarded as a manifestation of the effective stress principle, where the increase in pore pressure reduces the effective normal stress and brings a preexisting fault or intact rock mass to failure (*7*). Seismic slip requires failure to result in unstable slip, meaning that the resistance to sliding must decrease faster than the elastic unloading associated with fault slip. If a fault strengthens during slip, only aseismic creep should be possible. Only faults that weaken during sliding can, in principle, yield unstable slip. In general, the presence of fluids could either favor seismic slip, through thermal pressurization (*8*), or might impede seismic slip by a variety of other processes. In particular, dilatancy during slip could restrengthen the fault due to the resulting drop of pore pressure (*9*). Current models of earthquake nucleation (*10*) imply that slip becomes stable when the pore pressure approaches lithostatic, because the condition for stability (*10*) is then always reached. For slip to be unstable on a rate-weakening fault, the stiffness must be smaller than a critical value that has the effective normal stress at the numerator (*10*). If the effective normal stress goes to zero as pore pressure approaches lithostatic, this condition can never be met; slip should then be stable. Conditional stability might explain why aseismic slip has been inferred in some case studies (*4*, *11*, *12*). In reality, fault slip is coupled with fluid flow, and assessing whether seismic or aseismic slip should result from a fluid injection is a challenge.

We monitor a natural but initially inactive fault stimulated through a high-pressure injection of water, taking advantage of an instrument—the step-rate injection method for fracture in situ properties (SIMFIP) probe (*13*)—that allows the simultaneous measuring of fault-normal displacements, fault-parallel displacements, and fluid pressure. We selected a preexisting fault cutting through a carbonate formation accessible for examination and instrumentation thanks to an underground experimental facility located in southeastern France at a depth of 0 to 518 m (*14*). The fault is at least ~500 m long and trends 30°N 70°W. It cuts through porous grainstone carbonate layers (inner-platform Rudists' rich facies), with strike-slip to normal cumulated

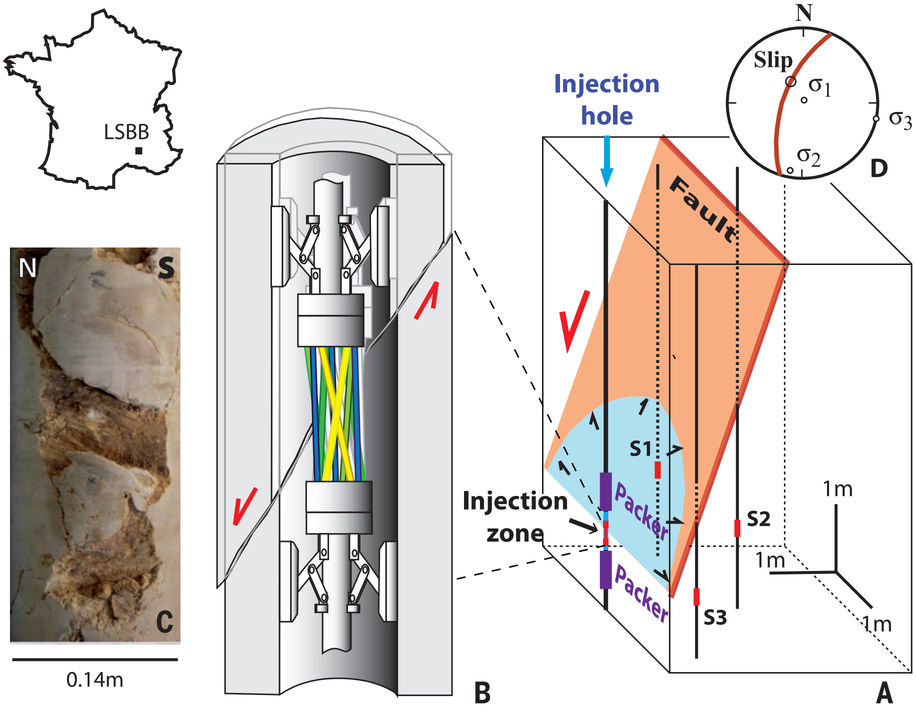

Fig. 1. Experiment setting. (**A**) Location of the injection interval and the seismometers (S1 to S3) in and around the fault plane. The experiment took place at a depth of 282 m below the Earth's surface, in cretaceous limestone of the southeast France sedimentary basin. (**B**) Schematic representation of the SIMFIP probe displacement sensor. Deformation of the linkage tubes (colored in yellow, green, and blue) captures the relative displacement of the anchors clamped on the borehole wall in each fault compartment (*16*). (**C**) Core from the main slip plane of the fault showing slickensided surfaces, breccia/gouge-rich zones, and a fractured damage zone. (**D**) Stereographic view of the state of principal stresses, the fault plane, and the fault-parallel slip vector induced by the experiment.

---

[1] Centre de Recherche et d'Enseignement de Géosciences de l'Environnement (UMR7330), University of Aix-Marseille, CNRS, IRD, 13545 Aix-en-Provence, France. [2] Géoazur (UMR 7329), University of Nice Sophia-Antipolis, CNRS, IRD, Côte d'Azur Observatory, 06560 Sophia-Antipolis, France. [3] Geological and Planetary Sciences, California Institute of Technology, Pasadena, CA 91125, USA. [4] Energy and Mineral Engineering and Geosciences, Earth and Mineral Sciences Energy Institute and G3 Center, Pennsylvania State University, University Park, PA 16802, USA.
*Corresponding author. E-mail: guglielmi@cerege.fr †Present address: Department of Earth Sciences, University of Cambridge, Cambridge, CB3 OEZ, UK.

Downloaded from www.sciencemag.org on June 17, 2015

slip of a few meters. The fault zone consists of subparallel fractures to 1- to 10-m length and discontinuous thin breccias (*15*). The in situ temperature at the location of the injection was 12.5°C and did not vary during the experiment. We therefore ignore thermal effects. We drilled a vertical well intersecting the fault at a depth of 282 m. Based on initial in situ measurements, the fault zone has an average initial permeability of 0.07×10^{-10} m^2 and a bulk modulus of 10 to 17 GPa that are a factor of 25 higher and 2 to 5 lower than the surrounding host rock, respectively (*16*). We injected water into a 1.5-m-long chamber between two inflatable packers spanning the fault zone (Fig. 1A). We injected a total of 950 liters of water with step-increasing rates while monitoring pressure, flowrate, fault movement in both shear and dilation (Fig. 1B), and seismicity (*16*) (fig. S1). We estimated the state of stress from hydraulic tests on preexisting fractures conducted at two different depths in adjacent boreholes using the hydraulic testing of preexisting fractures (HTPF) protocol (*17*) and taking into account topographic stresses. The maximum principal stress σ_1 = 6 MPa is subvertical and dips 80°S; σ_2 = 5 MPa is subhorizontal and strikes 0°N 20°E; and σ_3 = 3 MPa is subhorizontal and strikes 0°N 110°E (Fig. 1D).

Slip initiated at a pressure of about 1.5 MPa (S_0 in Fig. 2) with fault-parallel slip approximately parallel to the shear stress on the fault plane (Fig. 1C), consistent with reactivation by shear failure. No seismic event was detected until about 0.3 mm of fault slip, about 1100 s into the experiment. During this first stage, the dilation rate was around 6 μm/s and exceeded the fault slip rate, which was on the order of 4 μm/s. The dilation rates fell to about 20% of the slip rate approximately at the onset of seismicity. The slip rate increased to about 23 μm/s. The seismicity consists of impulsive micro-earthquakes and tremors (fig. S1), as is observed in injection experiments elsewhere (*18*). About 80 seismic events were generated at an average rate of 15 events per min. Half of these events occurred between 1100 and 1190 s before acceleration of fault slip (Fig. 2), and the transition from aseismic to seismic slip was not associated with any pressure variation (point S_S in Fig. 2). Both observations demonstrate that the majority of the seismic sources are located a few meters away from the injection point and may account for only a small fraction of the slip occurring on the fault segment where the fluid pressurization is occurring.

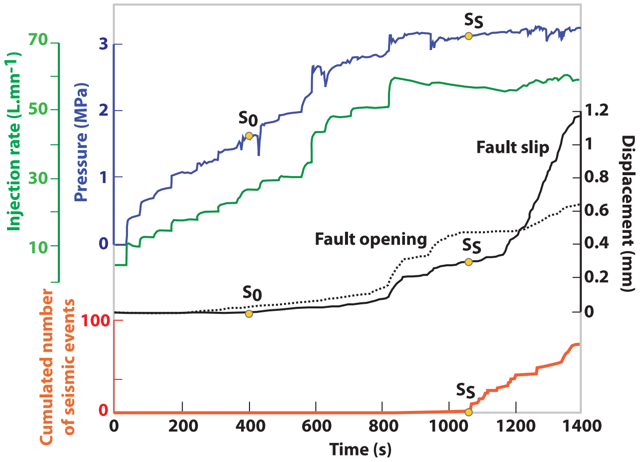

Fig. 2. Fault movements and seismicity induced over time by fluid injection. Temporal evolution of fluid pressure (blue), injection rate (green), fault slip (solid black line), normal displacement (dashed black line), and cumulative number of induced earthquakes (red) during the 1400-s-long injection. Slip initiates at S_0 = 400 s as pressure is increased to 1.5 MPa; seismicity initiates at S_s = 1100 s while there is no notable pressure variation.

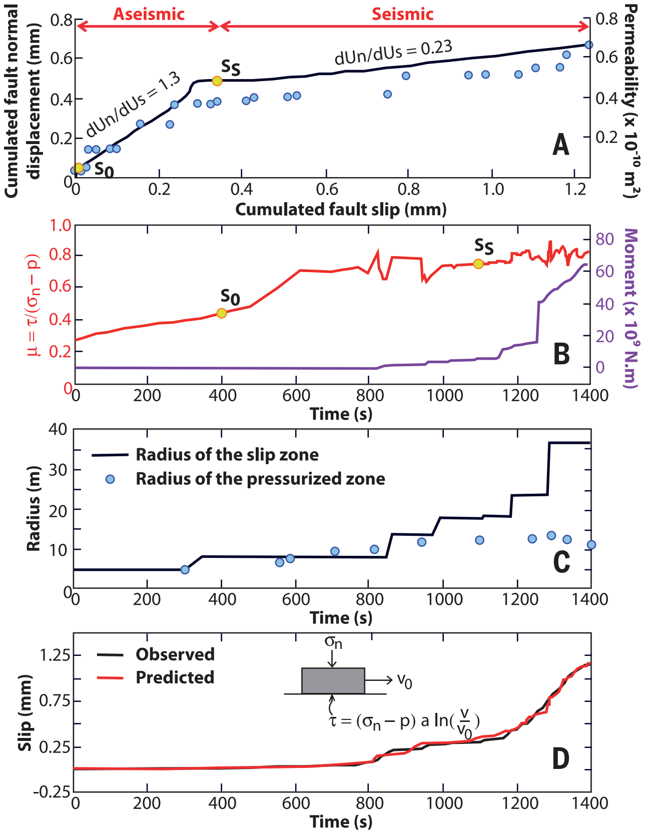

Fig. 3. Estimation of fault permeability and friction law from the in situ hydromechanical data. (**A**) Observed cumulative fault-normal displacement and modeled permeability (blue circles) versus observed fault slip (black). (**B**) Friction (orange), calculated based on the measurements of the initial stress and fault slip, and moment release (purple) derived from fault slip. (**C**) Comparison of the estimated radius of the sliding zone and of the pressurized zone. (**D**) Comparison of observed (black) and modeled (red) fault slip for the best-fitting rate-dependent friction law. The best-fitting friction law of the form $\mu = \mu_0 + a ln(v/v_0)$ has μ_0 = 0.67 and a = 0.0447, for a reference sliding velocity of $v_0 = 10^{-7}$m/s.

The observation that the fault opens during the injection implies that permeability varies in close relation to the evolution of fluid pressure, as suggested in theoretical and experimental studies (*19*, *20*). We used hydromechanical modeling (*21*) to determine the evolution of fault permeability (*16*). Our results show a 14-fold increase of the fault permeability from 0.07 to 1.0×10^{-10} m^2 during the aseismic period, representing about 70% of the cumulative permeability increase (20-fold) during the injection (Fig. 3A). This permeability increase probably results from the opening of fractures during sliding, possibly reflecting the roughness of the fracture walls and/or cataclasis of the fault rock and associated microcrack dilatation in the early stages of failure. The model indicates that the pressurized zone (defined here as the zone where the pore pressure exceeds 0.5 MPa) increases to about 12 m during the initial stage of completely aseismic slip (Fig. 3C).

We use our measurements to estimate the friction law and to determine whether aseismic slip is primarily due to rate-strengthening behavior or whether it is due to fluid pressurization bringing the fault zone to the domain of conditional stability. We approximate the sliding zone by a circular crack and assume quasistatic equilibrium with a complete shear stress drop [justified by the net opening of the fractures and following (*22*)]. This simple model ignores the pore-pressure gradient and viscous forces associated with fluid flow. With these assumptions, it is possible to calculate the crack radius as a function of time (Fig. 3C and fig. S3A), as well as the changes of shear and normal stresses associated with fault slip and dilation (*16*) (fig. S3, B and C).

The model yields an accumulated moment at the end of the experiment of $M_0 = 65 \times 10^9$ Nm, (equivalent to a moment magnitude M_w = 1.17), far larger than the moment released by the incremental microseismicity, which was estimated to be lower than −2 in magnitude; so slip is mostly aseismic in this experiment (Fig. 3B). Micro-earthquakes are triggered only when the estimated size of the slip zone exceeds the pressurized zone (Fig. 3C), suggesting that they occur off the pressurized zone. However, they might occur within the sliding zone or be triggered off the sliding area by static stress increase. Aftershocks might relate to afterslip in a similar way (*23*).

The ratio of the shear stress to the effective normal stress increases from about 0.4 to about 0.8 and indicates a friction between 0.6 and 0.8 once slip becomes notable (fig. S4). Qualitatively, this evolution correlates with slip rate better than with slip. The data suggest a logarithmically varying, rate-dependent friction, as frequently observed in laboratory measurements of rock friction (*24*) or derived from studies of afterslip following large earthquakes (*23*, *25*). We tested such a law based on a simple one-dimensional model (*16*). The model, which involves only two adjustable parameters, qualitatively fits the observations well (Fig. 3D). We determine the friction $\mu_0 = 0.67$ (+/−0.05) at a reference velocity of $v_0 = 0.1\ \mu\text{m/s}$, with a rate dependency of $a = \frac{\partial\mu}{\partial \ln v} = 0.0447$ (±0.005). We also tested rate-and-state friction laws (*16*) but found that the improvement was irrelevant in view of the uncertainties of the measurements. The friction coefficient increases to about 0.7 for slip rates of 1 to 20 μm/s. Similar values have been measured in the laboratory on faults formed in limestone and at comparable sliding rates (*26*–*28*). These laboratory experiments also show a rate-strengthening behavior at temperatures less than 100°C but a rate dependency at steady-state typically one order of magnitude lower than the value we obtained.

The aseismic behavior triggered by the fluid injection in this experiment is apparently due to an intrinsically rate-strengthening behavior, rather than to conditional stable creep of a rate-weakening fault. However, the seismicity, which was probably triggered outside the pressurized zone, requires some areas to allow earthquake nucleation, hence weakening during deformation. This observation is an indication that the frictional properties are likely heterogeneous, as supported by the observations of the main slip surface that displays gouge-rich zones and slickensided areas cutting solid rock (Fig. 1C). During the injection, the effective behavior is rate-strengthening. This behavior is possibly due to the fault zone being rate-strengthening on average, with the gouge-rich zones being possibly more rate-strengthening than the zones where the fault cuts solid rock (*27*) or because the rate-weakening asperities are brought to conditional stability by the increase in pore pressure. This interpretation could explain why seismicity is observed only when the crack radius has become larger than the radius of the pressurized zone. Our results prove unambiguously that fluid injection can trigger primarily aseismic slip, with seismicity induced as a secondary effect. This is observed in the context of our experiment, which is characterized by a particularly low effective normal stress. Thus, our results may be of particular relevance to seismic activity triggered at shallow depth by human-induced injections and shallow aseismic slip. Mechanism observed in this experiment could also be of relevance to explain natural processes at greater depth, such as deep afterslip, slow-slip events, and tremors.

REFERENCES AND NOTES

1. C. B. Raleigh, J. H. Healy, J. D. Bredehoeft, *Science* **191**, 1230–1237 (1976).
2. W. L. Ellsworth, *Science* **341**, 1225942 (2013).
3. C. Nicholson, R. L. Wesson, *Pure Appl. Geophys.* **139**, 561–578 (1992).
4. F. H. Cornet, H. Helm, H. Poitrenaud, A. Etchecopar, *Pure Appl. Geophys.* **150**, 563–583 (1997).
5. C. Nicholson, R. L. Wesson, Earthquake hazard associated with deep well injection: A report to the U.S. Environmental Protection Agency. *U.S. Geol. Surv. Bull.* 1951 (1990); http://pubs.usgs.gov/bul/1951/report.pdf.
6. E. Majer *et al*., *Geothermics* **36**, 185–222 (2007).
7. M. K. Hubbert, W. W. Rubey, *Geol. Soc. Am. Bull.* **79**, 115–166 (1959).
8. H. Noda, N. Lapusta, *Nature* **493**, 518–521 (2013).
9. P. Segall, J. Rice, *J. Geophys. Res.* **100**, 22155–22171 (1995).
10. C. Scholz, *Nature* **391**, 37–42 (1998).
11. S. Bourouis, P. Bernard, *Geophys. J. Int.* **169**, 723–732 (2007).
12. M. Zoback, A. Kohli, I. Das, M. McClure, The importance of slow slip on faults during hydraulic fracturing stimulation of shale gas reservoirs, SPE 155476, Society of Petroleum Engineers, Americas Unconventional Resources Conference, Pittsburgh, PA, 5 to 7 June 2012.
13. Y. Guglielmi *et al*., *Rock Mech. Rock Eng.* **47**, 303–311 (2014).
14. Laboratoire Souterrain à Bas Bruit, www.lsbb.eu
15. P. Jeanne, Y. Guglielmi, J. Lamarche, F. Cappa, L. Marie, *J. Struct. Geol.* **44**, 93–109 (2012).
16. Materials and methods are available as supplementary materials on *Science* Online.
17. B. C. Haimson, F. H. Cornet, *Int. J. Rock Mech. Min. Sci.* **40**, 1011–1020 (2003).
18. I. Das, M. Zoback, *Leading Edge (Tulsa Okla.)* **30**, 778–786 (2011).
19. J. Rutqvist, O. Stephansson, *Hydrol. J.* **11**, 7–40 (2003).
20. F. Cappa, Y. Guglielmi, J. Virieux, *Geophys. Res. Lett.* **34**, L05301 (2007).
21. F. Cappa, J. Rutqvist, *Int. J. Greenh. Gas Control* **5**, 336–346 (2011).
22. O. Scotti, F. H. Cornet, *Int. J. Rock Mech. Min. Sci. Geomech. Abstr.* **31**, 347–358 (1994).
23. H. Perfettini, J. P. Avouac, *J. Geophys. Res.* **109**, B02304 (2004).
24. C. Marone, *Annu. Rev. Earth Planet. Sci.* **26**, 643–696 (1998).
25. C. Marone, C. Scholtz, R. Bilham, *J. Geophys. Res.* **96** (B5), 8441–8452 (1991).
26. T. Tesei, C. Collettini, M. R. Barchi, B. M. Carpenter, G. Di Stefano, *Earth Planet. Sci. Lett.* **408**, 307–318 (2014).
27. B. M. Carpenter, M. M. Scuderi, C. Collettini, C. Marone, *J. Geophys. Res. Solid Earth* **119**, 9062–9076 (2014).
28. B. A. Verberne, C. R. He, C. J. Spiers, *Bull. Seismol. Soc. Am.* **100** (5B), 2767–2790 (2010).

ACKNOWLEDGMENTS

The experimental work was funded by the Agence Nationale de la Recherche (ANR) Captage de CO$_2$ through the HPPP-CO$_2$ project and by PACA through the PETRO-PRO project. The rate-and-state fault models for this study were supported by the French Academy of Sciences, the California Institute of Technology Tectonics Observatory, and the ANR HYDROSEIS under contract ANR-13-JS06-0004-01. We thank the SITES S.A.S. engineers H. Caron, C. Micollier, R. Blin, and H. Lançon, and the Petrometalic S.A. engineer J. B. Janovczyk, who jointly developed and operated the probe that enabled this experiment. We also thank the Laboratoire Souterrain à Bas Bruit (LSBB) engineers' team for their technical support during the installation of the experiment in one of the LSBB boreholes (www.lsbb.eu). Experimental data are available in the supplementary materials.

SUPPLEMENTARY MATERIALS

www.sciencemag.org/content/348/6240/1224/suppl/DC1
Materials and Methods
Figs. S1 to S6
References (*29*–*32*)
Database S1

3 March 2015; accepted 9 May 2015
10.1126/science.aab0476

NANOMATERIALS

A tunable library of substituted thiourea precursors to metal sulfide nanocrystals

**Mark P. Hendricks, Michael P. Campos, Gregory T. Cleveland,
Ilan Jen-La Plante, Jonathan S. Owen***

Controlling the size of colloidal nanocrystals is essential to optimizing their performance in optoelectronic devices, catalysis, and imaging applications. Traditional synthetic methods control size by terminating the growth, an approach that limits the reaction yield and causes batch-to-batch variability. Herein we report a library of thioureas whose substitution pattern tunes their conversion reactivity over more than five orders of magnitude and demonstrate that faster thiourea conversion kinetics increases the extent of crystal nucleation. Tunable kinetics thereby allows the nanocrystal concentration to be adjusted and a desired crystal size to be prepared at full conversion. Controlled precursor reactivity and quantitative conversion improve the batch-to-batch consistency of the final nanocrystal size at industrially relevant reaction scales.

The tunable electronic properties of nanometer scale crystals have inspired many synthetic methods that control crystal size and shape with extraordinary fidelity. Modern metal chalcogenide quantum dots, in particular, can be synthesized with a size that varies by less than a layer of surface atoms across the distribution. This precise control is afforded by the homogeneous nucleation and growth mechanism first described by LaMer and Dinegar to follow a three-phase sequence shown in Fig. 1A (*1*). In this mechanism, nucleation only occurs

Seismicity triggered by fluid injection–induced aseismic slip

Yves Guglielmi *et al.*

Science **348**, 1224 (2015);
DOI: 10.1126/science.aab0476

This copy is for your personal, non-commercial use only.

If you wish to distribute this article to others, you can order high-quality copies for your colleagues, clients, or customers by clicking here.

Permission to republish or repurpose articles or portions of articles can be obtained by following the guidelines here.

The following resources related to this article are available online at www.sciencemag.org (this information is current as of June 17, 2015):

Updated information and services, including high-resolution figures, can be found in the online version of this article at:
http://www.sciencemag.org/content/348/6240/1224.full.html

Supporting Online Material can be found at:
http://www.sciencemag.org/content/suppl/2015/06/10/348.6240.1224.DC1.html

A list of selected additional articles on the Science Web sites **related to this article** can be found at:
http://www.sciencemag.org/content/348/6240/1224.full.html#related

This article **cites 27 articles**, 6 of which can be accessed free:
http://www.sciencemag.org/content/348/6240/1224.full.html#ref-list-1

This article has been **cited by** 1 articles hosted by HighWire Press; see:
http://www.sciencemag.org/content/348/6240/1224.full.html#related-urls

This article appears in the following **subject collections:**
Geochemistry, Geophysics
http://www.sciencemag.org/cgi/collection/geochem_phys

Downloaded from www.sciencemag.org on June 17, 2015

Science (print ISSN 0036-8075; online ISSN 1095-9203) is published weekly, except the last week in December, by the American Association for the Advancement of Science, 1200 New York Avenue NW, Washington, DC 20005. Copyright 2015 by the American Association for the Advancement of Science; all rights reserved. The title *Science* is a registered trademark of AAAS.